Computers and Structures 256 (2021) 106637

Contents lists available at ScienceDirect

Computers and Structures

journal homepage: www.elsevier.com/locate/compstruc

Structural topology optimization of layout and raster angle for additive manufacturing technology with the shadow density filter

Gil Ho Yoon

School of Mechanical Engineering, Hanyang University, Seoul, South Korea

ARTICLE INFO

Article history:
Received 26 January 2021
Accepted 7 July 2021
Available online 30 July 2021

Keywords:
Topology optimization
Additive manufacturing
Raster angle optimization
Shadow density filter

ABSTRACT

The present research contributes in the structural topology optimization with the manufacturing limitation called the overhang constraint and the optimization of the anisotropic material properties. For the optimization with self-supporting structure, the overhang-free shadow filter method is developed. To consider the anisotropic material property, the raster angles of each layer (the printing direction used to print structures) are optimized simultaneously with topology. By adding the raster angles as the design variables, it is possible to find out optimal layouts as well as optimal raster angles considering the anisotropicity. Several numerical examples of compliance minimization problem are solved to demonstrate the validity and effectiveness of the present density filter and to show the importance of the raster angle.

1. Introduction

The present study develops a new topology optimization scheme considering the overhang constraint in the additive manufacturing and the raster angles of layers (see [1–8] and references therein). Despite some limitations and impediments, the additive manufacturing technology is becoming a preferred manufacturing technique in a variety of science and engineering as it can make innovative structural shapes and topologies which are impossible with previous manufacturing technologies without extra procedures or equipment instruments. Thus additive manufacturing is regarded as a flexible manufacturing tool for complex manifold structures. In addition, relevant researches reveal that mechanical parts deposed layer-by-layer show strong anisotropic material properties tremendously affecting the strength, stiffness, stability and usable service life and these properties should be considered in the designing process [9,10]. In addition, the manufacturing limitation of additive manufacturing technology brings new mathematical and engineering challenges but also new research opportunities. The structural topology optimization with the manufacturing limitation and the optimization of the anisotropic material properties are considered here. The overhang constraint is treated as a geometrical constraint and imposed by developing a new density filter method. Among some available filters, the shadow density filter is modified in order to impose the overhang constraint [11]. To consider the anisotropic material property, the raster angles of each layer are optimized simultaneously with topology as shown in Fig. 1(b). By setting the raster angles as the design variables, it is possible to find out optimal layouts as well as optimal raster angles considering the anisotropicity.

Many innovative researches regarding the overhang constraint exist. As reviewing all the relevant researches is almost impossible, it is our suggestion to look up recent review papers regarding the overhang constraint in topology optimization [1–7,12–16]. In [4,5], some reviews regarding the additive manufacturing in structural optimization were reported. In [2,3,6,7,16], the topology optimization methods considering the additive manufacturing limitations are proposed. The application of the structural topology optimization was proposed in [1,8,17,18]. Due to the geometric limitation of the additive manufacturing, the maximum length scale control as well as the overhang angle control should be considered (see [8,13] and references therein). In the consideration of the structural optimization for additive manufacturing, an interesting topic is to develop the overhang-free topology optimization, i.e., totally the remove of the need for supporting structure. The overhang-free indicates that all overhang angles are larger than the minimum self-supporting angle. The consideration and formulation of these overhang constraints have been one of actively researching topics in structural optimization as it requires a substantial development in theory and implementation. The topological optimization results are simply postprocessed to remove the overhang-free violations [19]. By reformulating an optimization formulation by either adding constraints or applying a density filtering, overhang free designs can be obtained [5,19–21]. In [20], the overhang free designs are achieved by the design variable projection method. In [3], the density filter method was proposed to

E-mail address: ghy@hanyang.ac.kr

https://doi.org/10.1016/j.compstruc.2021.106637
0045-7949/

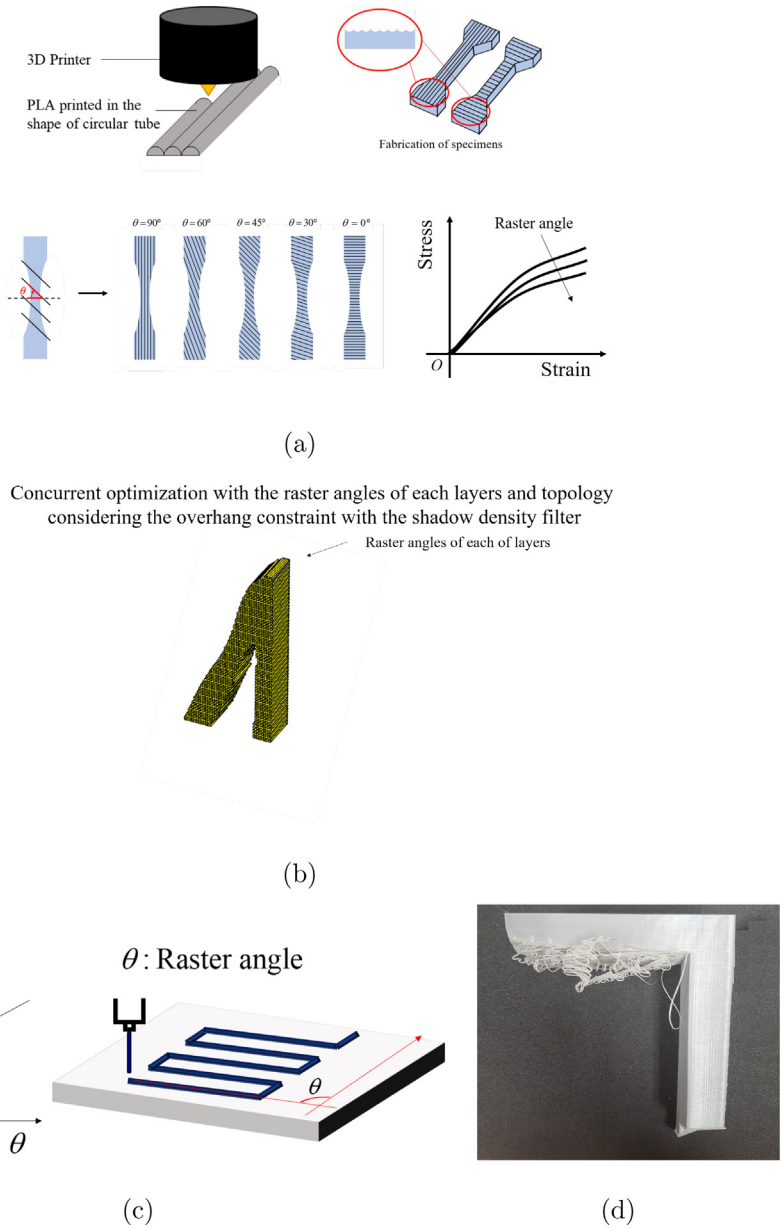

Fig. 1. Concurrent optimization with the raster angles of each of layers and topology considering the overhang constraint with the shadow filter. (a) The material properties depending on the raster angle, (b) a topology optimization with the concurrent optimization of the raster angles and topology, (c) the raster angle of the additive manufacturing and (d) the fallen surface due to the overhang constraint.

consider the overhang free design. In [22], the PUP (Projected Undercut Perimeter) constraint was added to the optimization formulation and the concept of the self-supporting structure was demonstrated and validated. In [6], the structural boundary normal to the optimum and intermediate designs with zigzag and blurry boundaries were estimated and formulated to impose the overhang constraint. In [21], the application of the topology optimization considering the overhang constraint was applied for automotive application. In [23], the overhang constraint was considered for the structural optimization for compliant mechanism. The overhang constraints were also implemented in the framework of the MMC (Moving Morphable Component) and MMV Moving Morphable Void approaches [24]. As the geometry information is used in the design process, the building orientation of additive manufacturing can be proposed with the pareto levelset method too. In [14], the structural topology optimization reducing supporting structures is developed. In [15], the overhang constraint and the minimum member size are considered in topology optimization for the additive manufacturing. In [25], the additive manufacturing infill structure was optimized for buckling load [1]. The raster angles are also considered in structural optimization [9,10]. As the material properties of printed structure are typically anisotropic, the overall stiffness is influenced by the building direction or the raster angle [9]. In [10], the optimization of the effective properties of the constitutive material of structure is considered. First of all, they introduced a simple model for the anisotropic feature and they optimize in-fill structure. They observed the existences of various patterns to fill internal structure such as anisotropic crust with isotropic bulk or anisotropic bulk, offset model and isotropic crust with infill. Many relevant researches for structural optimization for additive manufacturing exist.

The objective of the present study is not to compete with the novel topology optimization methods considering the overhang constraints to obtain self-support design. Rather this research

studies the importance of the consideration of the anisotropicty with the overhang constraint imposed with the extended shadow filter [11]. Additive manufacturing technologies make us enable to produce 3 dimensional products by building up layers of material. An additive manufacturing process comprises several steps. First of all a first layer of building material is formed at a substrate. After printing and solidification, a new melted material layer is dispensed again to add another layer in the previous layer covering an overhang area. These procedures are repeated to form a structure with consolidation material or light activated material depending on the type of the additive manufacturing technology. When the overhang angle is smaller than a certain value, the melted and dispensed layer drops and some supporting structures should be added as shown in Fig. 1(b). Without the help of the supporting structure, it is hard to manufacture complex structure or some additional postprocessing procedure is required. Then the supporting structures should be ripped out to leave the main structure. One pitfall of this postprocessing approach may be that the surfaces between the supporting structures and the main structure will be rough and less clean finished. To avoid additional supporting structures and postprocessing which increase the cost and deteriorate the surface finish, several relevant researches exist in structural optimization to assure the self-supporting structure [1–6]. To address this issue, this research presents the concept of the shadow density filter to impose the overhang constraint. Thus, it is intended that the overhang constraint should be considered during the topology optimization process. In order to consider this manufacturing constraint, the present research employs the shadow density filter which was developed to consider the molding or the milling constraint [11]. The idea of the shadow density filter is to impose the manufacturing constraint by the density filter simulating the shadow of structure. The density values of the topology optimization become the absorption coefficients and they are multiplied to each other to simulate the shadowing phenomenon and to impose the molding constraint in topology optimization [11]. This research modifies the direction of the virtual light from the parallel path to the omni-direction path. By controlling the penetration depth and the direction of the virtual light, this research finds out that it is possible to impose the overhang constraint.

Structures printed by the additive manufacturing technology inevitably embrace in-fill structures and layers as shown in Fig. 1. These printing patterns or meso-structures are observed at the outer surface (crust) as well as the internal structure (in-fill structure). These printing patterns are varied and determined by the employed process conditions in the additive manufacturing and it has been experimentally and theoretically reported that the material properties such as Young's modulus, shear modulus, Poisson's ratio, and strength show some variations as illustrated in Fig. 1(a) (see [9,10] and references therein). Indeed, during an optimization process, the effect of the raster angle can be considered and this research sets the raster angles as the additional design variables in topology optimization. Fig. 1(b) shows the idea of the present research optimizing the topology and raster angles of layers. It is also possible to add or remove the outer structure called the crust as shown in Fig. 2. The actually printed structures with and without the crust are shown in Fig. 2(b, c). In the present study, it is assumed that the printed parts does not have the crust and their material properties are bulk as shown in Fig. 2(c).

The paper is organized as follows. Section 2 provides some backgrounds to the topology optimization and the overhang constraint with the expanded shadow density filter. In Section 3, several optimization studies are presented. A two dimensional problem is presented to show the application of the shadow density filter for the overhang constraint. The importance and characteristics of the raster angles in the additive manufacturing technology are considered in several three dimensional problems. Section 4 provides the conclusions and suggestions for future research topics.

2. Topology optimization formulations

2.1. Topology optimization with the manufacturing constraint

This research considers topology optimization minimizing compliance subject to mass constraint based on the SIMP interpolation function. The finite element formulation is employed to solve the equilibrium equation with the anisotropic or orthotropic material property defined on the printing plane on the analysis domain Ω as follows:

$$\nabla \cdot \boldsymbol{\sigma}(\mathbf{u}) + \mathbf{b} = \mathbf{0} \text{ in } \Omega \tag{1}$$

where the nominal stress tensor, the displacement field vector, and the body force are denoted by $\boldsymbol{\sigma}, \mathbf{u}$, and $\mathbf{b}$, respectively. In the present study, the self-weight is not considered. The Neumann boundary condition on $\partial\Omega_N$ and the Dirichlet boundary condition on $\partial\Omega_D$ are defined as follows:

$$\boldsymbol{\sigma} \cdot \mathbf{n} = \mathbf{f} \text{ on } \partial\Omega_N, \ \mathbf{u} = \mathbf{0} \text{ on } \partial\Omega_D \tag{2}$$

where the normal vector is denoted by $\mathbf{n}$ and the traction force is denoted by $\mathbf{f}$. The stresses, $\boldsymbol{\sigma}$, and the strains, $\boldsymbol{\varepsilon}$, are related as follows:

$$\boldsymbol{\sigma} = \mathbf{C}\varepsilon \tag{3}$$

The linear anisotropic or orthotropic constitutive matrix is denoted by $\mathbf{C}$. (In the present study, the orthotropic material property is considered for the material property but the anisotropic material property can be applied.) For the topology optimization problem considering the raster angles and the overhang constraint with the shadow density filter, the following optimization problem is formulated and solved.

$$\begin{aligned} &\underset{\mathbf{x}}{\text{Minc}} = \mathbf{F}^{\mathrm{T}}\mathbf{U} + \alpha \sum \boldsymbol{\gamma} \\ &\text{Subject to } \mathrm{V}(\tilde{\boldsymbol{\gamma}}) \leqslant \mathrm{V}* \\ &\mathbf{K}(\tilde{\boldsymbol{\gamma}}, \boldsymbol{\theta})\mathbf{U} = \mathbf{F}, \tilde{\boldsymbol{\gamma}} = \Phi(\boldsymbol{\gamma}), \Phi : \text{Modified shadow filter} \\ &\mathbf{X} = [\boldsymbol{\gamma}, \boldsymbol{\theta}] = [\gamma_1, \gamma_2, \gamma_3 \ldots \gamma_{nel}, \theta_1 \ldots \theta_{\text{layer}}] \\ &\boldsymbol{\gamma}_{\min} \leqslant \boldsymbol{\gamma} \leqslant 1, -\pi \leqslant \boldsymbol{\theta} \leqslant \pi \end{aligned} \tag{4}$$

where the stiffness matrix, the displacement vector and the force vector are denoted by $\mathbf{K}, \mathbf{U}$ and $\mathbf{F}$, respectively. The linear elasticity is applied with the orthotropic material properties. The objective function summing the compliance and the penalization is denoted by c. The design variables defining topology are denoted by $\boldsymbol{\gamma}$ varying from a lower value $\boldsymbol{\gamma}_{\min}$ to ones. The filtered design variable with the shadow density filter, Φ, considering the manufacturing limitation is $\tilde{\boldsymbol{\gamma}}$. The number of finite elements is denoted by *nel* and the number of layers in the printing direction is denoted by *layer*. The volume and the upper volume are denoted by V and V$*$, respectively. As the extended shadow filter can find out some intermediate design variables for topologically optimized structure, the summation of the design variable is added to the objective function with the scaling factor α to remove the intermediate design variables. The penalization α should be chosen to make the design variables converged but not too high to make an unwanted local optimal. In the present study, the factor is chosen to have about 10 percent of the compliance. Considering the linear strain, the equilibrium equations are constructed as follows:

$$\mathbf{K}(\tilde{\boldsymbol{\gamma}}, \boldsymbol{\theta})\mathbf{U} = \mathbf{F}, \mathbf{K}(\tilde{\boldsymbol{\gamma}}, \boldsymbol{\theta}) = \sum_{e=1}^{nel} \mathbf{k}_e(\tilde{\gamma}_e, \theta_{\text{layer of element}}) \tag{5}$$

The corresponding raster angle of each element is denoted by $\theta_{\text{layerofelement}}$. The constitutive matrix becomes a function of the ras-

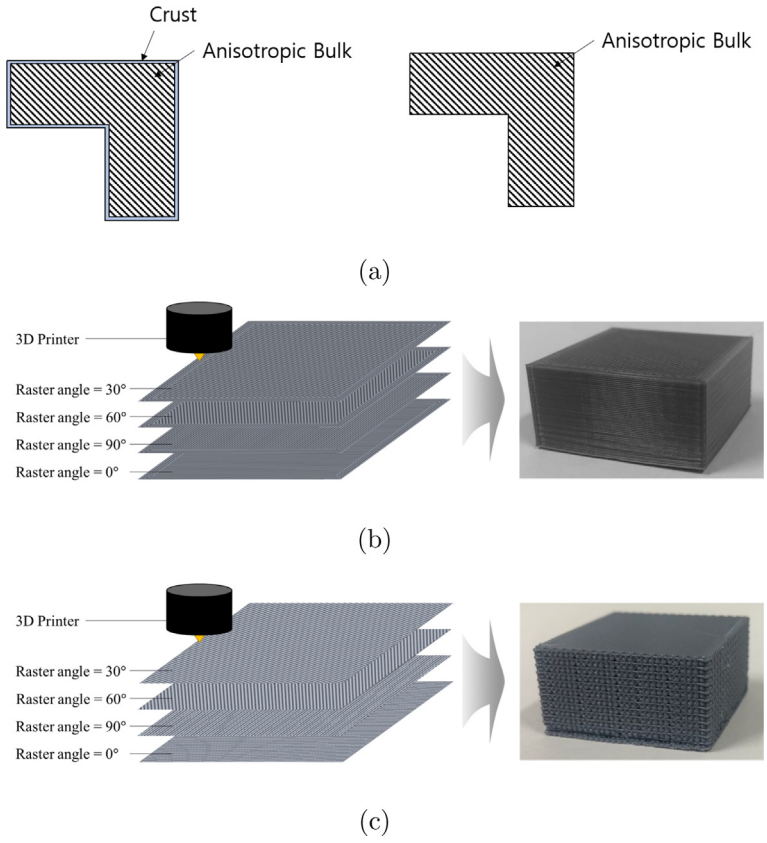

Fig. 2. Crust and internal structure. (a) Printing method with crust and anisotropic or orthogonal internal bulk and raster angle, (b) an example of a 3d printing structure with the crust and (c) an example of a 3d printing structure without the crust.

ter angle of each element. To formulate this, the compliance tensor **S**, i.e., the inverse tensor of the constitutive tensor **C**, is defined as follows:

$$\mathbf{S}=\begin{bmatrix} \frac{1}{E_x} & -\frac{\nu_{yx}}{E_y} & -\frac{\nu_{zx}}{E_z} & 0 & 0 & 0 \\ -\frac{\nu_{xy}}{E_x} & \frac{1}{E_y} & -\frac{\nu_{zy}}{E_z} & 0 & 0 & 0 \\ -\frac{\nu_{xz}}{E_x} & -\frac{\nu_{yz}}{E_y} & \frac{1}{E_z} & 0 & 0 & 0 \\ 0 & 0 & 0 & \frac{1}{2G_{yz}} & 0 & 0 \\ 0 & 0 & 0 & 0 & \frac{1}{2G_{xz}} & 0 \\ 0 & 0 & 0 & 0 & 0 & \frac{1}{2G_{xy}} \end{bmatrix}, \boldsymbol{\sigma}=\{\sigma_{xx},\sigma_{yy},\sigma_{zz},\sigma_{yz},\sigma_{xz},\sigma_{xy}\} \tag{6}$$

$$\text{Symmetric condition}: \frac{\nu_{xy}}{E_x}=\frac{\nu_{yx}}{E_y},\frac{\nu_{yz}}{E_y}=\frac{\nu_{zy}}{E_z},\frac{\nu_{zx}}{E_z}=\frac{\nu_{xz}}{E_x} \tag{7}$$

where the Young's moduli at each direction are denoted by E_x, E_y and E_z, respectively. For the orthotropic material, the symmetric conditions are imposed. In the simulation, the three Young's moduli and the three Poison's ratios, ν_{yx}, ν_{zx} and ν_{yz}, are prescribed and the other Poisson's ratios are determined considering the symmetric condition. The subscripts can be 1,2 and 3 without the loss of generality. The Poisson's ratios are denoted by ν_{xy}, ν_{xz} and ν_{yz}, respectively. The shear moduli are defined by G_{xy}, G_{xz}, and G_{yz}, respectively. They are determined by $G_{xy}=\frac{E_x}{2(1+\nu_{xy})}, G_{xz}=\frac{E_y}{2(1+\nu_{xz})}$, and $G_{yz}=\frac{E_z}{2(1+\nu_{yz})}$. The constitutive tensor or the inverse of the compliance tensor, **S**, with the rotational matrix is defined as follows:

$$C'_{mnop}=R_{mi}R_{nj}R_{ok}R_{pl}C_{ijkl} \tag{8}$$

For our finite element implementation, the above constitutive matrix is obtained with the matrix formulation considering the order of the strain and the stress components in (6) [26,27]. For example, the y-direction rotational matrix with the rotational angle θ is defined as follows:

$$\mathbf{R}=\begin{bmatrix} c^2 & 0 & s^2 & 0 & 2cs & 0 \\ 0 & 1 & 0 & 0 & 0 & 0 \\ s^2 & 0 & c^2 & 0 & -2cs & 0 \\ 0 & 0 & 0 & c & 0 & -s \\ -cs & 0 & cs & 0 & c^2-s^2 & 0 \\ 0 & 0 & 0 & s & 0 & c \end{bmatrix}, c=\cos(\theta), s=\sin(\theta) \tag{9}$$

$$\mathbf{C}'=\mathbf{RCR}^{\mathrm{T}} \tag{10}$$

The material property in the linear elasticity equation is interpolated with respect to the density variables, $\boldsymbol{\gamma}$ as follows:

$$\mathbf{C}(\tilde{\boldsymbol{\gamma}},\boldsymbol{\theta})=\mathbf{C}'\tilde{\boldsymbol{\gamma}}^n \tag{11}$$

where the rotated constitute matrix is $\mathbf{C}'$, and the penalization factor of the SIMP interpolation function is denoted by n. This research adopts 3 or 4 for this penalization factor value. With the raster representation of the optimized layouts in the framework of the SIMP method, the gray elements can cause the unwanted patterns and the inaccurate apex angle measurement. With a sufficient higher penalization of the SIMP method, the design variables tend to converge to solids and voids. The density filters including the present shadow density filter remove some unwanted patterns during the optimization process. With the gradient based optimizer, the sensitivity values of the objective and the constraint with respect to the density of the e-th element, γ_e, should be computed as follows:

$$\frac{dc}{d\gamma_e} = \frac{dc}{d\tilde{\gamma}}\frac{d\tilde{\gamma}}{d\gamma_e} = \frac{dc}{d\tilde{\gamma}}\frac{d\Phi(\boldsymbol{\gamma})}{d\gamma_e}, \frac{dc}{d\tilde{\gamma}_e} = -\mathbf{u}_e^{\mathrm{T}}\frac{d\mathbf{k}_e}{d\tilde{\gamma}_e}\mathbf{u}_e \tag{12}$$

The sensitivity of the volume constraint with respect to the element density, γ_e, can be similarly obtained with the chain rule.

$$\frac{dV}{d\gamma_e} = \frac{dV}{d\tilde{\gamma}}\frac{d\tilde{\gamma}}{d\gamma_e} = \frac{dV}{d\tilde{\gamma}}\frac{d\Phi(\boldsymbol{\gamma})}{d\gamma_e} \tag{13}$$

The sensitivity of the objective function with respect to the raster angle of each layer can be obtained as follows:

$$\frac{dc}{d\theta_{layer}} = -\sum_e \mathbf{u}_e^{\mathrm{T}}\frac{d\mathbf{k}_e}{d\theta_{layer}}\mathbf{u}, e \in \{\text{All elements defined by } \theta_{layer}\} \tag{14}$$

The sensitivity of the volume with respect to the raster angle is set to zero.

2.2. Development of the shadow density filter

This subsection presents a new development of the shadow density filter to impose the overhang constraint of the additive manufacturing technology. Our previous contribution of the shadow density filter was intended to impose the molding manufacturing limitation in topology optimization [11]. The idea of the shadow filter is to simulate the physical phenomenon of absorbing and smearing from light and implement this idea in topology optimization. Rather than solving extra additional physics equations, this approach uses the density filtering to limit the design space compatible to the molding manufacturing approach. In our previous contribution, it was assumed that the light travels parallel. In the current study, the omnidirectional light in limited and controlled directions is proposed to impose the overhang constraint.

The shadow filter does simulate the absorption of light on materials. Light penetrates materials depending on the porosity of materials and here finite elements represent materials. Porosity is defined as a fraction of the volume of voids over the total volume or the design variables in topology optimization in (4). Thus, light is more absorbed with materials or finite elements containing low porosity. With materials containing high porosity, light is less absorbed. With the simple summation and multiplications of the design variables, the shadow filter simulates these light absorption processes in order to impose the manufacturing constraint in topology optimization. In our previous contribution [11], the light travels parallel for the molding constraint and this research modifies the direction and penetration depth of light in order to impose the self-supporting condition.

Inspired from the relevant researches [1–6], this research also presents a new approach in the framework of the shadow density filter. Fig. 3 shows the idea of the shadow filter for the overhang constraint. In these figures, the red triangular boxes are representing the areas of the light penetrations. The finite element at the top of the triangle is affected by the light emitted from the elements beneath the corresponding element. For example, in Fig. 3(b), the top element rendered by the gray color is formulated as follows:

$$\tilde{\gamma}_{ij} = \gamma_{ij} \times (1 - (1 - \gamma_{i-1,j+1}) \times (1 - \gamma_{ij+1}) \times (1 - \gamma_{i+1,j+1})) \tag{15}$$

The idea of the above formulation is that the filtered design variable, $\tilde{\gamma}_{ij}$, is determined not only by γ_{ij} but also the combinations of the three elements underneath the (i,j)th element. The second part of the right side of the formulation simulates the absorption of light due to the porosities of the four elements. With zeros for $\gamma_{i-1,j+1}, \gamma_{ij+1}$ and $\gamma_{i+1,j+1}$, the second part becomes zero. Indeed, regardless of the γ_{ij}, the filtered design variable, $\tilde{\gamma}$, becomes zero. On the other hand, the term $(1-(1-\gamma_{i-1,j+1})\times(1-\gamma_{ij+1})\times(1-\gamma_{i+1,j+1}))$ becomes one when any of the $(i-1,j+1)$th, $(i,j+1)$th, or $(i+1,j+1)$th elements becomes one. Indeed, the filtered gamma $\tilde{\gamma}_{ij}$ becomes one when γ_{ij} and any of the three elements underneath the (i,j) th element become ones as shown in Table 1.

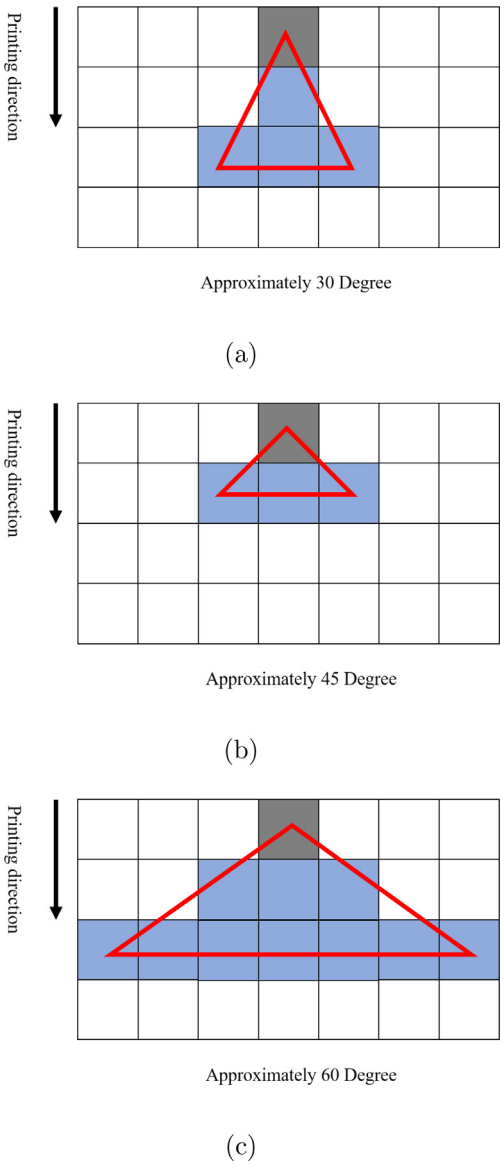

Fig. 3. The concept of the shadow density filter in two dimensional space (The weighted factor of the densities underneath the top element is multiplied to the design variable.): (a) the shadow for the 30° overhang constraint, (b) the shadow for the 45° overhang constraint and (c) the shadow for the 60° overhang constraint.

The developed formulation can be implemented to impose the 45° overhang constraint in topology optimization. Compared with the other existing approaches using the pseudo min-max operators, the operations are formulated with simple algebra operators. The number of layers underneath the corresponding element can

Table 1
The filtering example of the 45° overhang constraint in (15).

$\tilde{\gamma}_{ij}$	γ_{ij}	$(\gamma_{i-1,j+1}, \gamma_{ij+1}, \gamma_{i+1,j+1})$
1 (Solid)	1	(1,0,0), (0,1,0), (0,0,1) (1,1,0), (1,0,1), (0,1,1) (1,1,1)
0 (Void)	1 or 0	(0,0,0)
0 (Void)	0	Any combination

be varied depending on the purpose. In the present study, we consider one or two layers to illustrate the concept of the shadow density filter. After the above operation, it is possible to use the S-shape function to accelerate the optimization process [28]. The formulations can be extended for the other overhang angles as shown in Fig. 3(a) for the approximately 30° overhang constraint or Fig. 3(c) for the approximately 60° overhang constraint. The formulations for these overhang constraints can be listed as follows:

$$\tilde{\gamma}_{i,j} = \gamma_{i,j} \times \theta_{absorp30} \text{ for } 30^\circ \text{ overhang} \tag{16}$$
$$\theta_{absorp30} = 1 - (1 - \gamma_{i,j+1}) \times (1 - \gamma_{i-1,j+2}) \times (1 - \gamma_{i,j+2}) \times (1 - \gamma_{i+1,j+2})$$

$$\tilde{\gamma}_{i,j} = \gamma_{i,j} \times \theta_{absorp45} \text{ for } 45^\circ \text{ overhang} \tag{17}$$
$$\theta_{absorp45} = 1 - (1 - \gamma_{i-1,j+1}) \times (1 - \gamma_{i,j+1}) \times (1 - \gamma_{i+1,j+1})$$

$$\tilde{\gamma}_{i,j} = \gamma_{i,j} \times (1 - \theta^{L_1}_{absorp60} \times \theta^{L_2}_{absorp60}) \text{ for } 60^\circ \text{ overhang} \tag{18}$$

$$\theta^{L_1}_{absorp60} = (1 - (1 - \gamma_{i-1,j+1}) \times (1 - \gamma_{i,j+1})) \times (1 - \gamma_{i+1,j+1}))$$
$$\theta^{L_2}_{absorp60} = (1 - (1 - \gamma_{i-3,j+2}) \times (1 - \gamma_{i-2,j+2}) \times (1 - \gamma_{i-1,j+2}) \times (1 - \gamma_{i,j+2}) \times (1 - \gamma_{i+1,j+2}) \times (1 - \gamma_{i+2,j+2}) \times (1 - \gamma_{i+3,j+2}))$$

For the self-supporting conditions of 30° or 60°, the design variables of the two layers underneath the corresponding element are considered. To illustrate the defined operators, Fig. 4 shows several examples of the extended shadow filter with the testing structure generated randomly to show the effect of the shadow density filter. As illustrated, the extended shadow filter can successfully impose the overhang manufacturing constraints when the structures are converging to ones or zeros.

One important aspect in the present density filter is that the optimization algorithm is smart in terms of finding some intermediate density distributions in order to make the filtered density an optimal topology without the overhang constraint. In order to remove this side effect, it is possible to add/constrain the summation of the design variables or add/constrain the convergence of the design variables with $\sum \gamma \times (1 - \gamma)$. In addition, it is possible to insert some penalization factors to the above formula to improve the convergence. The above filters can be extended into 3 dimensional structure too with the following formulation for the 30° overhang constraint.

$$\tilde{\gamma}_{i,j,k} = \gamma_{i,j,k} \times (1 - \gamma_{i,j,k+1}) \times \prod (1 - (\gamma_{s,m,k+2})) \tag{19}$$
$$s \in \{i-1, i, i+1\}, m \in \{j-1, j, j+1\}$$

For the density filter with the 45° overhang constraint, the following filtered density can be formulated. Fig. 5 shows the schematic diagram of this operator for the 45° overhang constraint and other examples with the different overhang angles can be obtained similarly.

$$\tilde{\gamma}_{i,j,k} = \gamma_{i,j,k} \times \prod (1 - (\gamma_{s,m,k+1})) \tag{20}$$
$$s \in \{i-1, i, i+1\}, m \in \{j-1, j, j+1\}$$

For the density filter with the 60° overhang constraint, the following density can be formulated.

$$\tilde{\gamma}_{i,j,k} = \gamma_{i,j,k} \times \prod (1 - (\gamma_{s,m,k+1})) \times \prod (1 - (\gamma_{p,q,k+2})) \tag{21}$$
$$s \in \{i-1, i, i+1\}, m \in \{j-1, j, j+1\}$$
$$p \in \{i-2, i, i+2\}, q \in \{j-2, j, j+2\}$$

Fig. 6 shows some examples of the filter in 3 dimensional structures. Fig. 6(a) is a structure to considered. As it is assumed that the printing is carried out in the y-direction, the center block cannot be manufactured without the supporting structure. Thus, the layouts in Fig. 6 are the post-processed layouts satisfying the overhang constraints with the present formula. To consider the raster angles of the additive manufacturing process, it is possible to modify the extended shadow filter with the finite element procedure with anisotropic material property. In the present study, it is assumed that each layer perpendicular to the printing direction has an equal raster angle and an equal material property. With the raster represen-

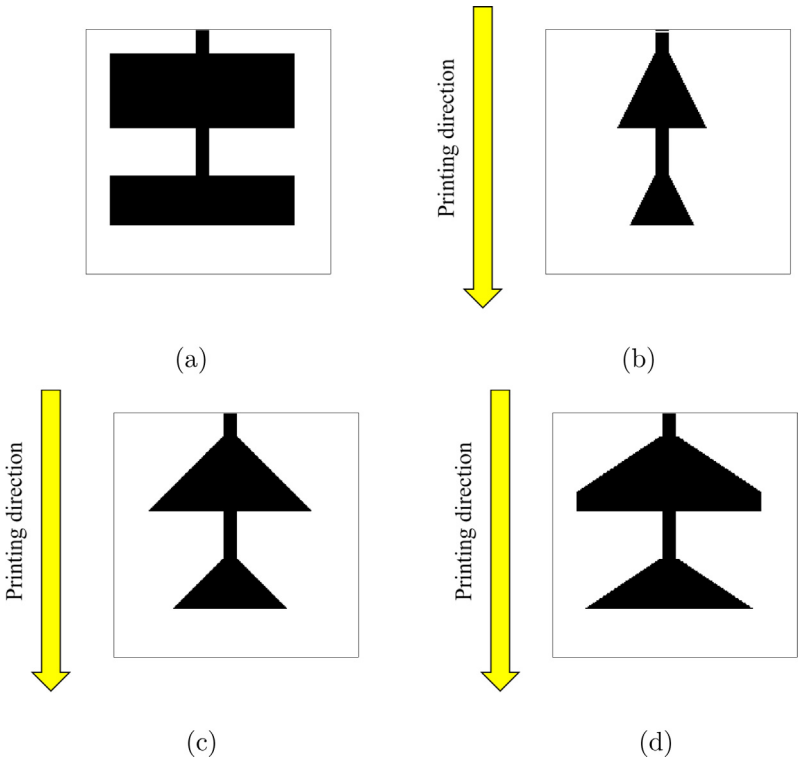

Fig. 4. The shadow density filter example in 2 dimensional space. (a) The structure of interest, (b,c and d) the filtered designs with the 30°, 45° and 60° overhang constraints, respectively.

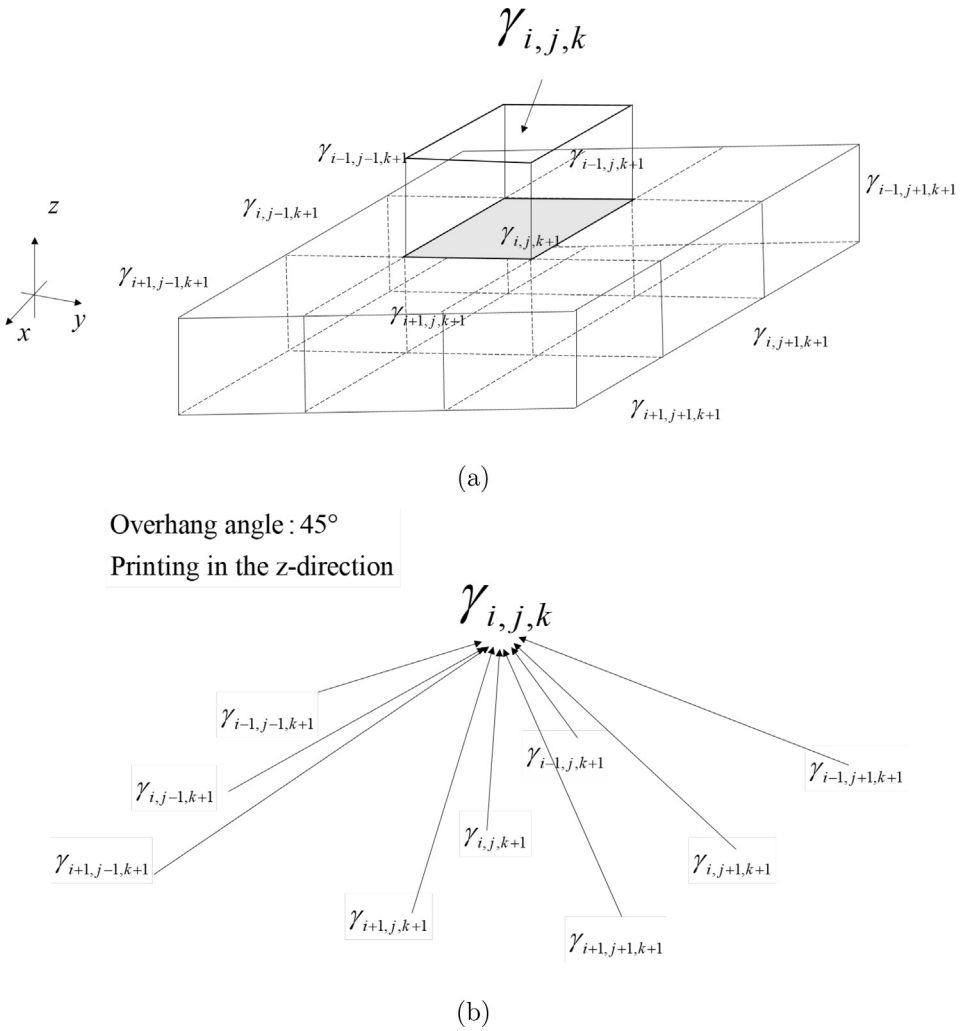

Fig. 5. The shadow density filter for the 3 dimensional 45° overhang constraint: (a) the design variables and (b) the shadowing of the design variables.

tation of the optimized layouts in the framework of the SIMP method, the gray elements can cause the unwanted patterns and the inaccurate apex angle measurement. With a sufficient higher penalization of the SIMP method, the design variables tend to converge to solids and voids. Thus, the density filters including the present shadow density filter remove some unwanted patterns during the optimization process.

3. Optimization results

To validate the concept of structural topology optimization considering the manufacturing constraint with the shadow density filter (self-supporting structure), this section solves one 2-dimensional problem and several 3-dimensional problems. The geometries and the material properties of the considered problems are arbitrary chosen to show the validity of the present research. The consideration of the self-weight has not been considered in the finite element simulation. For the optimization algorithm, the method of moving asymptotes (MMA) algorithm is used [29].

3.1. 2 Dimensional example: the application of the overhang constraint (Self-supporting structure)

First of all, in order to show the effectiveness of the extended shadow density filter for the self-supporting structure, the structural optimization in Fig. 7 is considered with the isotropic linear material; the raster angle optimization should be carried out in 3 dimensional space. Without the overhang constraint for the self-supporting concept, the optimized layout can be obtained in Fig. 7(a:right). The postprocessed designs shown in Fig. 7(b) indicate that the design in Fig. 7(a) becomes inferior by imposing the overhang constraint assuming the printing direction from top to bottom. This aspect has initiated many relevant researches. In order to show the application of the overhang constraint with the extended shadow density filter, Fig. 8 shows the optimization results with the 30°, 45° and 60° overhang constraints. It is assumed that the printed part and layers grow downward. The left figures show the distributions of the design variables $\boldsymbol{\gamma}$ whereas the right figures show the filtered densities $\tilde{\boldsymbol{\gamma}}$ used for the stiffness matrix. As illustrated, the extended shadow density filters can impose the manufacturing constraints successfully with the extended shadow filter. The results satisfying the overhang constraints or the geometric constraints, the compliance values become higher. The shadow density filters with 30 degrees and 60 degrees have the filters formulated with the three layers when the shadow density filter with 45 degrees has the two layers. Due to this aspect, gray elements appear often with the shadow density filters with 30 degrees and 60 degrees. These optimized structures illustrate the application of the shadow density filter to impose the condition of the self-supporting structure. As the shadow density filter removes the unwanted patterns violating the overhang constraint, the designs are local optima. As the original optimization

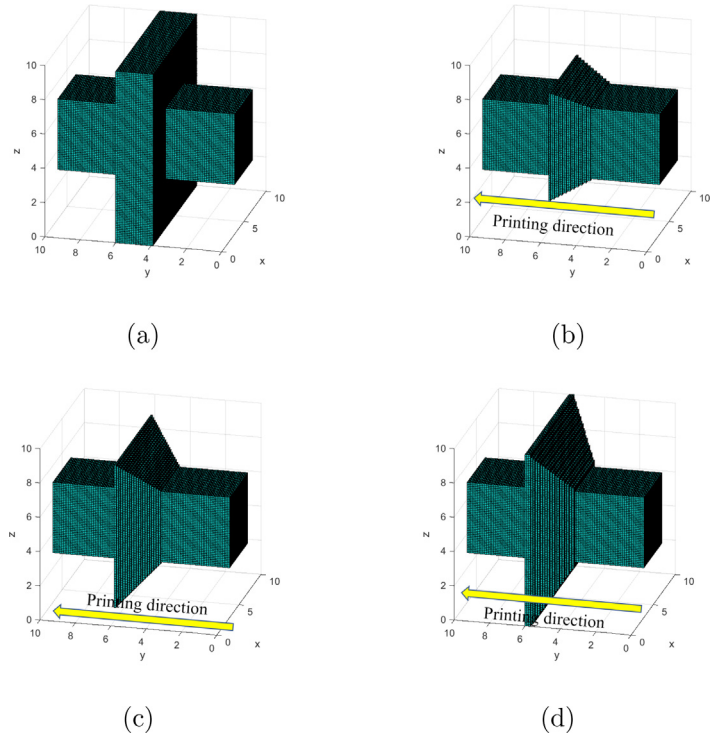

Fig. 6. The shadow density filter example in 3 dimensional space. (a) The structure of interest, (b,c and d) the filtered designs with the 30°, 45° and 60° overhang constraints, respectively.

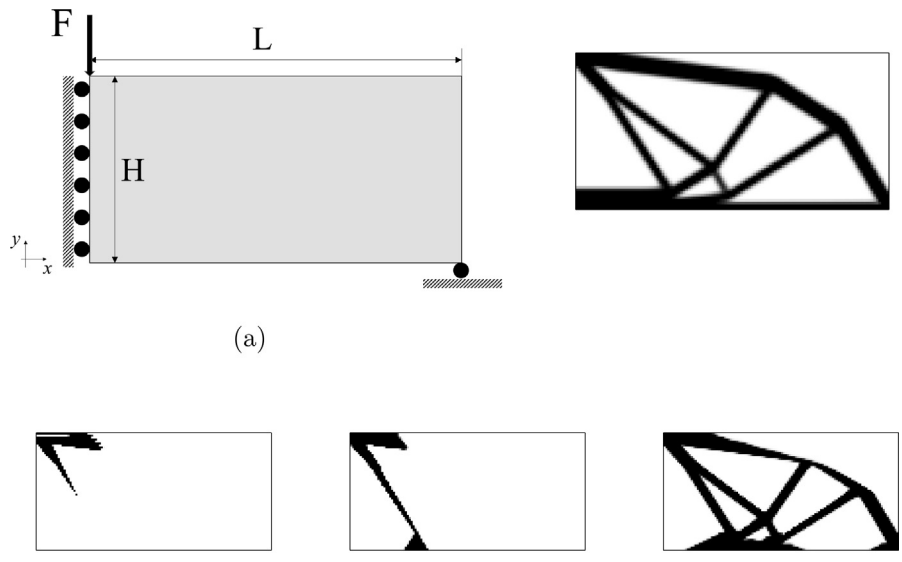

Fig. 7. Two dimensional compliance minimization problem. (a) Problem definition (L = 120 m by H = 60 m, Young's modulus = 1 N/m^2, Poisson's ratio = 0.3, 120 by 60 discretization, F = 0.5 N Mass constraint: 30%, Printing direction: from top to bottom) and an optimization without the constraint (Compliance: 32.8941 (J)) and (b) the postprocessed optimal designs (non-sensible compliance values for the left and the center designs due to the disconnection between the load and the bottom boundary condition and the compliance of the right design: 1497 (J)).

formulation pursuits an optimized layout minimizing the compliance subject to the mass constraint, the designs satisfying the overhang constraint with the density filter are local optima. To alleviate this issue, it is possible to add additional constraints to the optimization formulation. However, the removal of a specific pattern may require a lot of local constraints and a computational time. Thus, the present study achieves this purpose by the present shadow density filter.

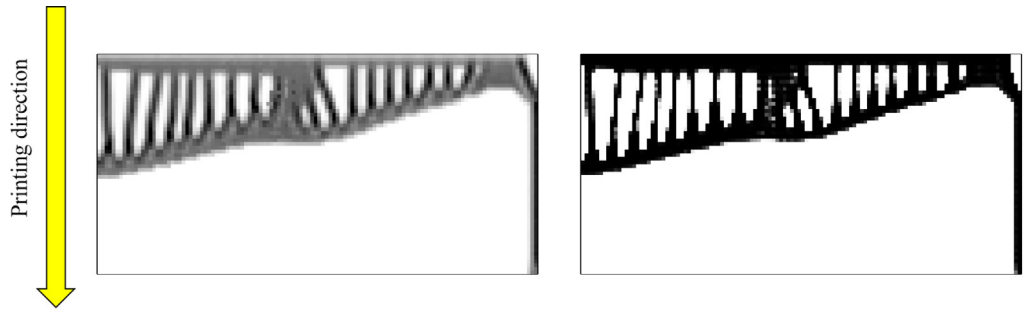

(a) (Left: design variable, right: physical density)

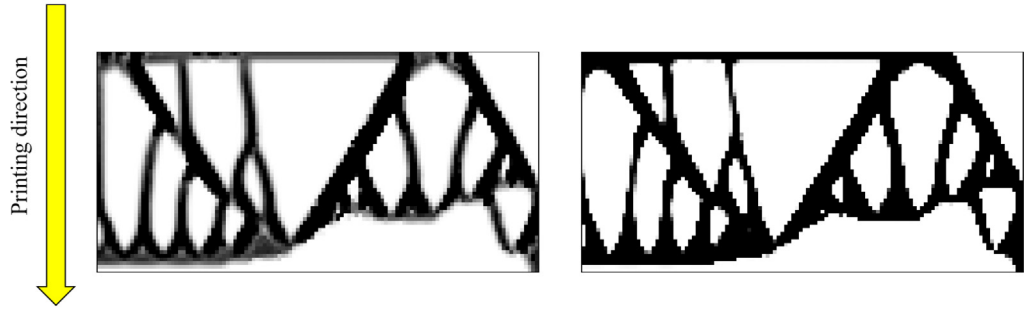

(b) (Left: design variable, right: physical density)

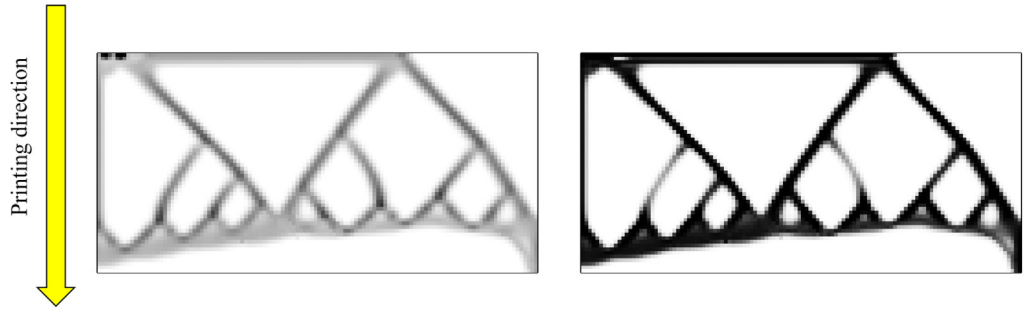

(c) (Left: design variable, right: physical density)

Fig. 8. The optimized self-supporting layouts with the overhang constraint but without the optimization of the raster angle (left: the design variable γ, right: the filtered density variable $\bar{\gamma}$). (a) An optimized layout with the 30° overhang constraint (Compliance: 217.3242 (J)), (b) an optimized layout with the 45° overhang constraint (Compliance: 179.2713 (J)) and (c) an optimized layout with the 60° overhang constraint (Compliance: 78.1591 (J)).

3.2. 3 dimensional example: optimization of raster angles only

For the next example, the optimization problems of the raster angles of each layer of the box manufactured and printed by the additive manufacturing are considered to call into question the value and importance of the consideration of the anisotropicity of printed parts. The box domain is set to 5 m by 5 m by 10 m with the uniform pressure at the top of the box and the fixed and clamped boundary condition for the bottom of the box in Fig. 9. The design domain is discretized by 5 elements in the x-direction by 30 elements in the y-direction by 5 elements in the z-direction. Note that the domain and the finite element discretization are arbitrarily chosen for the illustration purpose. To investigate the effect of the material properties and the geometry, an orthotropic material and a set of elastic constants are employed; Without the loss of generality, the Young's moduli for the 1-direction, the 2-direction and the 3-direction are set to $1\,N/m^2$, $5\,N/m^2$, and $1\,N/m^2$, respectively. The Poisson's ratio $v_{21} = v_{31} = v_{23} = 0.3$. Without rotation, the 1,2 and 3 direction become the x,y and z directions. The symmetric compliance matrix is defined. Hence, the considered material is a linear orthotropic material obeying the Hooke's law. By rotating the material around the y-direction, i.e., the printing direction of the additive manufacturing, the purpose of the optimization problem is to find out the distribution of the raster angles to maximize the stiffness and minimize the compliance. To achieve this, the topological design variables, $\boldsymbol{\gamma}$, are set to ones in the optimization problem in (4). Not permitting the change of the material status from void to solid or vice versa within the solid box, the raster angles of each layer are optimized through the gradient optimizer. The initial raster angles of each layer are set to 0°. It is assumed that the additive manufacturing technology maintains the raster angles of each layer. To get a guideline or a reference to compare optimized results of the gradient based optimizer, Fig. 9right) shows the curve of the compliance value by varying the raster angles. The raster angles of the 30 layers in the y-direction are assumed to be identical for the compliance evaluation in Fig. 9right). The approximately shifted cosine curve is obtained and it turns out that the minimum compliance is $4.744 \times 10^{-}3$ (J) at 45°. From a physical point of view, it is interpreted that the setting of the raster angles

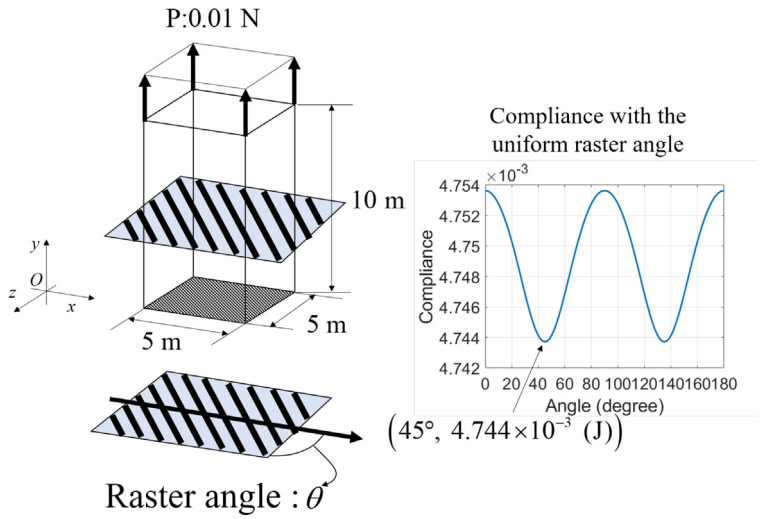

Fig. 9. Example of the uniform raster angle.

to 45° or 145° increases the overall stiffness of the solid box. Fig. 10 (a) shows the optimized raster angles for 30 layers; The number of the design variables of the raster angles is 30. As the raster angles of each layer can be optimized, interestingly the raster angles of the layers below 5 m and above 9 m are far from 45° and the raster angles in the middle of the box are about 45°. To provide a deeper understanding of the physical aspect of this distribution, a functional evaluation would be highly desirable. By investigating the curve, it is found that the Saint-Venant's principle can be utilized

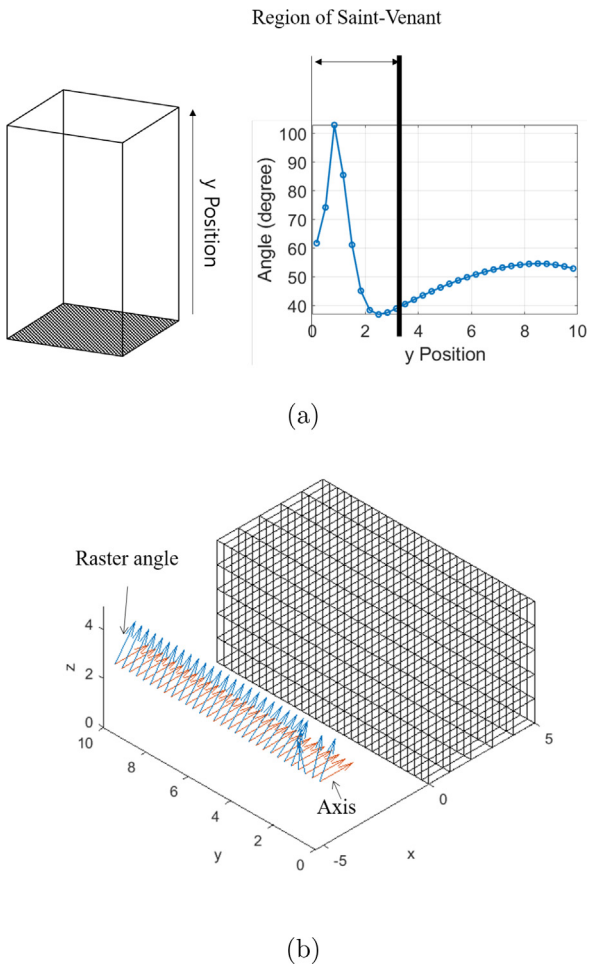

Fig. 10. Example of the uniform raster angle (objective: 4.7410 × 10^{-3}(J)).

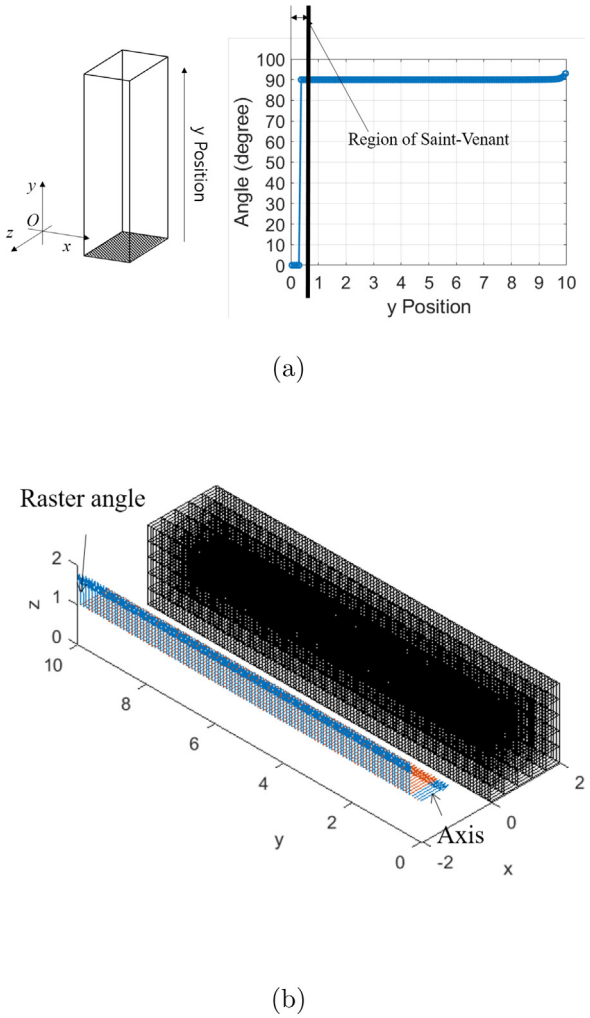

Fig. 11. Example of uniform angle with the z-direction force (Objective: 21.4110 (J)).

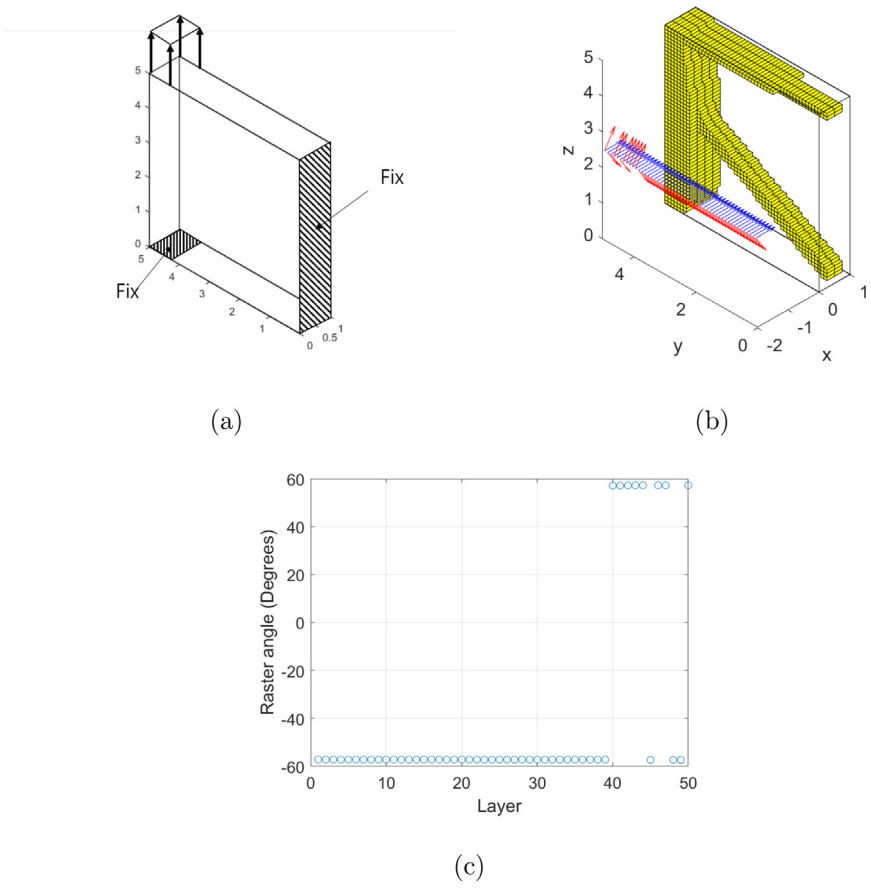

Fig. 12. Example 2: Optimization with the raster angles of each layer and topology. (a) The problem definition, (b) the optimal design without any geometric constraint and the raster angle distribution (Compliance: 3.6787×10^3 (J)), and (c) the raster angles.

to explain the optimized result. The optimization algorithm determines the raster angles considering the effect of the fixed boundary condition and the raster angles below 5 m are far from 45°. To represent the optimized raster angles, Fig. 10(b) shows the box structure and the directions of the raster angles of each layer; the red arrows are the vectors pointing the x-direction and the blue arrows are the vectors of the optimized raster angles. The compliance of the optimization design is 4.7410×10^{-3} (J) which is mediocre and is slightly lower than that in Fig. 10(a) (4.744×10^{-3} (J)). The improvement of the objective function to the worst compliance is about 5 percent and this improvement is dependent on the directional differences in the employed material properties. To investigate the effect of the size of the design domain, Fig. 11 shows the optimization with the narrow box (2 m by 10 m by 2 m). The domain is discretized with 5 by 120 by 5 elements and the forces are applied in the z-direction. Accordingly, the number of the raster angles of the layers is 120 in this example. By assuming the uniform raster angles along the y-direction again, the lowest compliance is about 21.4733 (J) at 90°. Fig. 11(b) shows the optimized raster angles whose compliance value is slightly improved to 21.4110 (J). This is also smaller than that of the design with the uniform raster angle. The Saint-Venant's principle is also applied here.

3.3. 3 dimensional example 1: The optimization with the raster angle and the topological design variables

In order to investigate the effect of the optimization of the raster angles of each layer and topological design variables, the 3-dimensional design problem in Fig. 12(a) is considered. The size of the design domain is 1 m by 5 m by 5 m and the right side and the fraction of the bottom surface are clamped. The z-direction force is applied. Fig. 12(b) shows the optimization result without any manufacturing constraint. The arrows beside the optimal topology represent the reference bases along the x-direction (blue arrows) and the directions of the optimized raster angles of each layer (red arrows). As in the previous examples, it is assumed that the finite elements at the same y-position have the uniform raster angles printed by the additive manufacturing. As the vertical force in the z-direction can be resisted by a vertical structure with the help of the bottom fixed boundary condition, the vertical structure in the z-direction appears mainly. Due to the effect of the Poisson's ratio, the top horizontal bar structure and the oblique bar structure appear in order to utilize the supporting condition of the right side at y = 0. Without the support of the right side of the box, a main vertical structure connecting the force and the fixed boundary condition of the bottom surface is an optimal design. Note that the raster angles of each layer are optimized simultaneously. The structural members in the middle of the design domain have about −57 and 57° for the raster angles. Due to the orthotropic property, the alignments of these two different angles are same. Due to the effect of the clamped boundary condition, the intersection regions show some variations of the raster angles. This example illustrates that not only the optimal topology but also the raster angles of each juxtaposed layer can be optimized to increase the stiffness or minimize the compliance. However, due to the overhang constraint in the additive manufacturing technique, the vertical bar cannot be printed when the layers are juxtaposed in the y-direction. Thus, this obtained structure is the

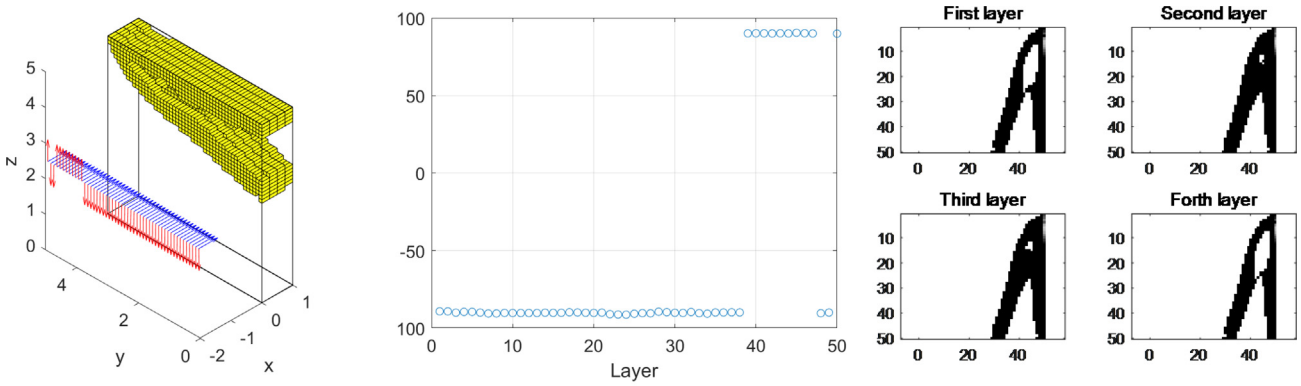

(a) Overhang constraint: 30°

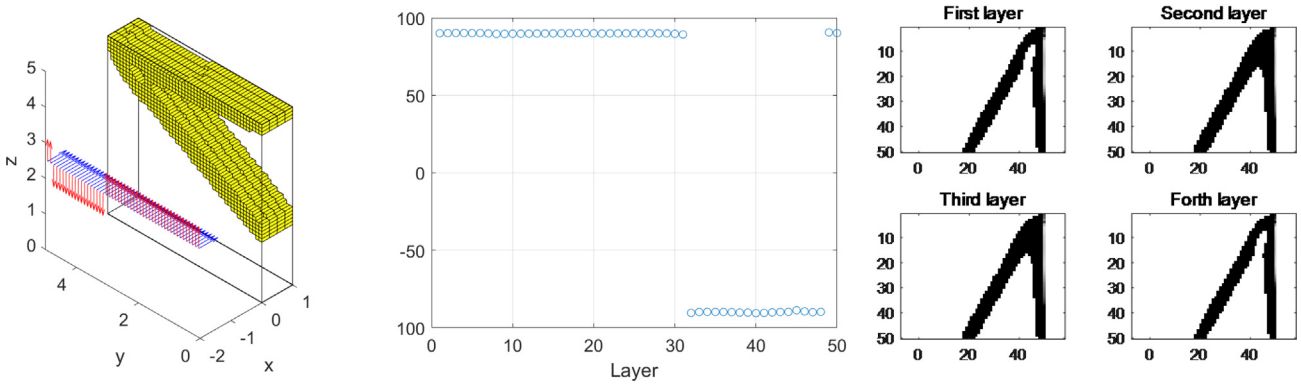

(b) Overhang constraint: 45°

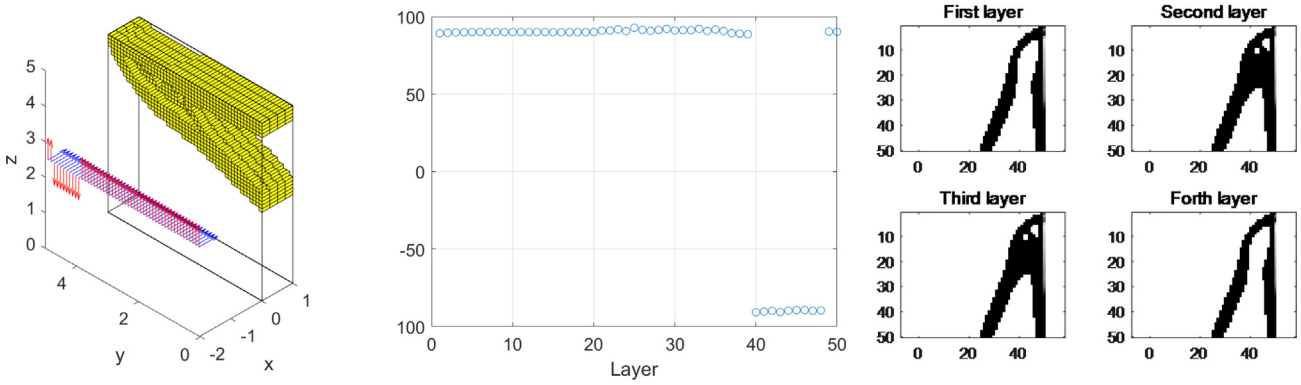

(c) Overhang constraint: 60°

Fig. 13. The optimization results with the present shadow density filter. (See Table 2 for the objective values, blue arrows: the directions with 0 degree, red arrows: the directions with the optimized raster angles.).

Table 3
The objective values of the optimal layouts with the different material property in Fig. 14.

	Optimal design in Fig. 14 and postprocessed designs (J)	Optimal designs in Fig. 14 with the overhang constraint (J)
Without overhang constraint	1.5952×10^3	
Overhang constraint (30°)	2.5870×10^7	4.9869×10^4
Overhang constraint (45°)	2.5971×10^7	3.5387×10^4
Overhang constraint (60°)	9.2544×10^5	2.5392×10^4

Table 2
Comparison of the optimized designs (Fig. 12 and Fig. 13) with the shadow density filter.

	Optimal design in Fig. 12 and postprocessed designs (J)	Optimal designs in Fig. 13 with the overhang constraint (J)
Without overhang constraint	3.6787×10^3	
Overhang constraint (30°)	5.6385×10^7	6.3701×10^4
Overhang constraint (45°)	6.3975×10^7	3.2495×10^4
Overhang constraint (60°)	1.1257×10^6	4.9229×10^4

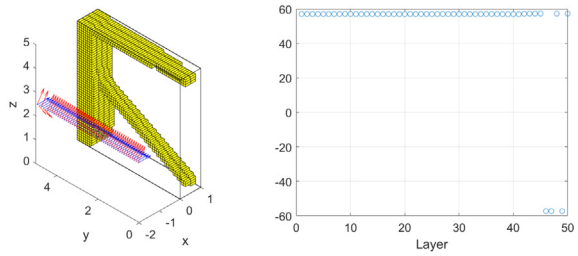

(a) Without the overhang

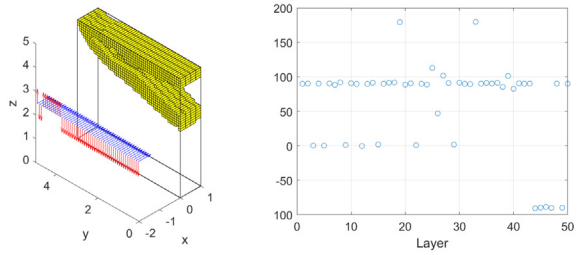

(b) Overhang constraint: 30°

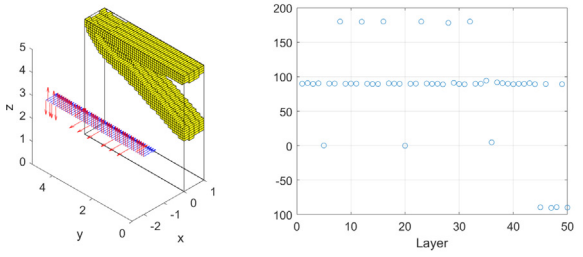

(c) Overhang constraint: 45°

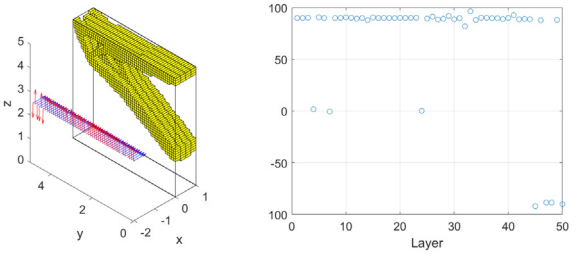

(d) Overhang constraint: 60°

Fig. 14. Optimal layouts with the different material property ($E_1 = 14.7$ N/m^2, $E_2 = 1$ N/m^2, $E_e = 0.735$ N/ m^2, $v_{12} = 0.292$, $v_{21} = 0.019864$, $v_{13} = 0.4490$, $v_{31} = 0.02245$, $v_{23} = 0.3900$, $v_{32} = 0.53061$, $G_{12} = 0.9410$ N/m^2, $G_{31} = 0.449$ N/m^2, $G_{23} = 0.3900$ N/m^2).

optimized design in terms of the compliance but not for the manufacturing constraint. To consider the overhang constraint or the self-supporting condition, it is assumed that the layers are printed in the y-direction from the bottom layer to the upper layer. Then the overhang constraints, i.e., 30°, 45°, and 60°, are applied for the optimal topologies in Fig. 13. With the shadow density filter for the additive manufacturing, the vertical bar connecting the load to the fixed boundary condition of the bottom surface disappears as the vertical bar mainly violates the overhang constraint when this structure is printed in the y-direction. The representations of the optimized raster angles are shown beside of the optimized structures. The optimized angles are about 90 and −90 degrees for the 30° overhang constraint (Fig. 13(a)), the 45° overhang constraint (Fig. 13)) and the 60° overhang constraint ((Fig. 13(c)). To show the structures, the postprocessing is carried out and the densities without the postprocessing at each cross section are plotted in the figures. Table 2 compares and cross checks the compliance values of the optimized structures in Fig. 12 and Fig. 13. The second column shows the objective value without the shadow density filter and the objective values after applying the overhang constraints. The objective value without the overhang constraint but with the optimization of the raster angle (Fig. 13) is 3.6787×10^3 (J) and the compliance values with the overhang constraints are dramatically changed to 5.6385×10^7 (J), 6.3975×10^7 (J) and 1.1257×10^6 (J) in cooperating with the overhang constraints; the lower bound of the constitutive matrix is set to 10^{-3} times of the constitutive matrix of the solid material. With the overhang constraints, the compliance values are higher than the compliance value without the overhang constraint. However, after the postprocessings with the shadow density filters, the compliance values are significantly deteriorated (see the second column in Table 2). In addition, as the present shadow density filter imposes the manufacturing constraint or the geometric constraint, the obtained designs should be interpreted as the local optima. To impose the overhang constraints for 30° and 60°, the design variables of the three layers are linked when the design variables of the two layers are used for the overhang constraints for 45° (see the formulations and equations (19), (20) and (22)). Due to the local optima issue casused by these differences, it is observed that the compliance value of the design with the 45° overhang constraint is better than the compliance value of the design with the 60° overhang constraint as expected. This can be explained by the local optima issue of the present shadow density filter. Locally optimized layouts of the compliance minimization problem may be similar to the layout in Fig. 12. In other words, the optimization formulation finds out an optimal design or optimal designs with a higher compliance value(s),as the present density filter or the shadow density filter limits the design space in which the optimizer should explore. Indeed, the more restrictive your design space is, the more local optimized layouts you can get. The detail objective values are listed in Table 2.

In order to test the effect of the material properties, the effect of another material property on the optimal layout and the optimal raster angle is considered in Fig. 14. The shear moduli are deter-

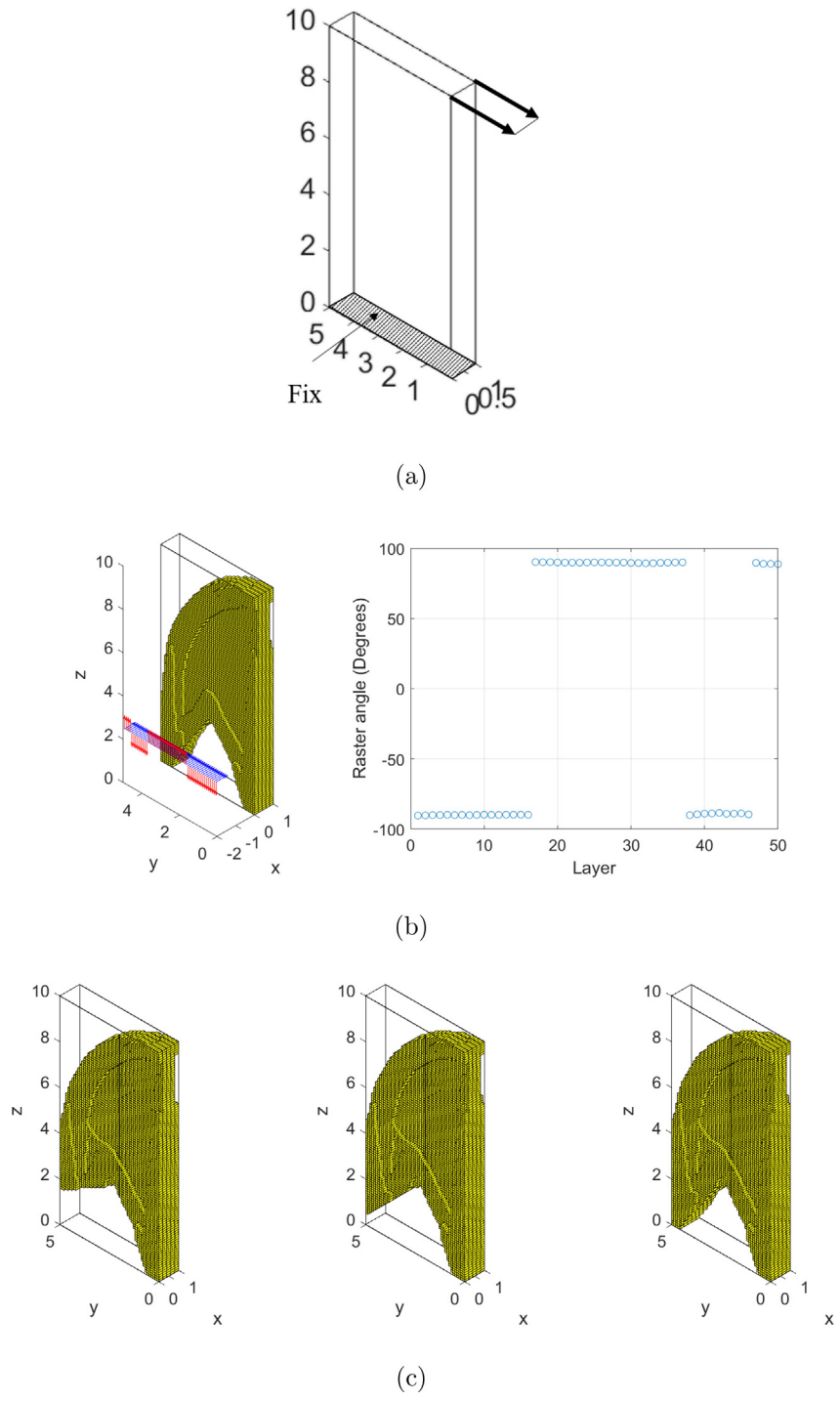

Fig. 15. Example 2–1: (a) the problem definition (1 m by 5 m by 10 m), (b:left) the optimal layout with 40 percentage mass (Compliance: 3.3478×10^4 (J)) and (b:right) the optimized raster angle distribution and (c) the postprocessed designs considering the overhang constraints (Left: the design with 30 degree overhang angle (Compliance: 1.6184×10^6 (J)), Middle: the design with 45 degree overhang angle (Compliance: 1.6203×10^6 (J), Right: the design with 60 degree overhang angle (Compliance: 3.4051×10^4 (J))).

mined independently in the considered material. The overall topological shapes are similar with some differences in detail. However, the distribution of the raster angles are different. With the different material orientation, the enhancement of a specific layout is often accompanied by optimizing the different raster angle. This example also illustrates the importance of the optimization of the raster angle. The detail objective values are listed in Table 3.

3.4. 3 dimensional example 2: the optimization with the raster angle and the topological optimization design variables

As the next example, the solid box (1 m by 5 m by 10 m) is considered in Fig. 15(a) with the same material properties in the previous example. The bottom surface is clamped and the load is applied at the end of the domain. First of all, the optimization pro-

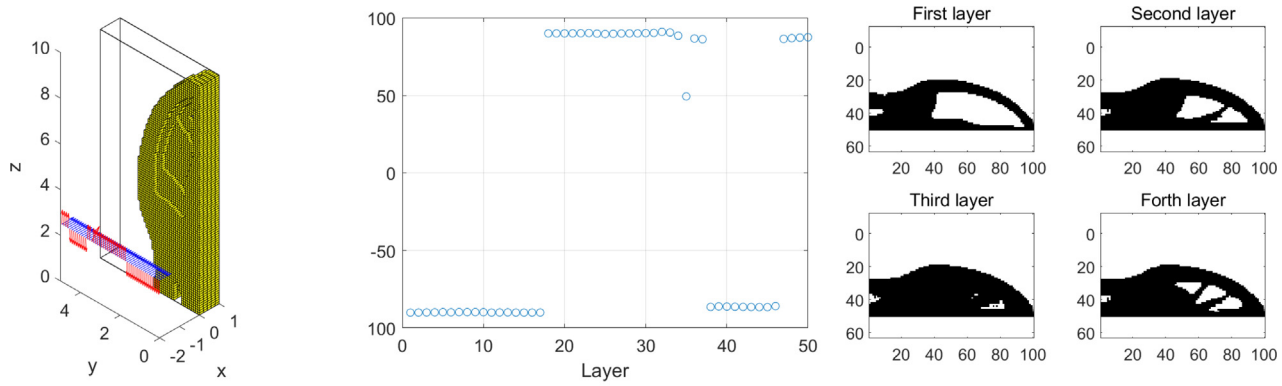

(a) Overhang constraint: 30°

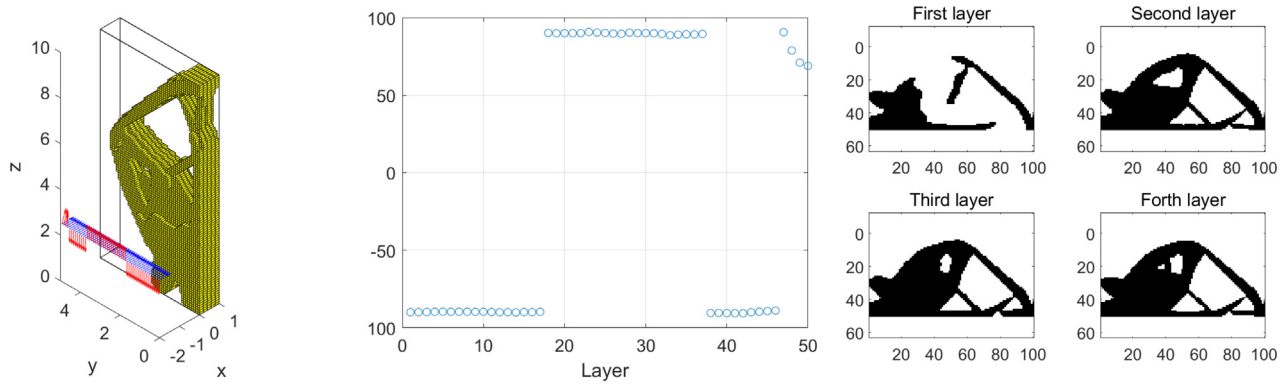

(b) Overhang constraint: 45°

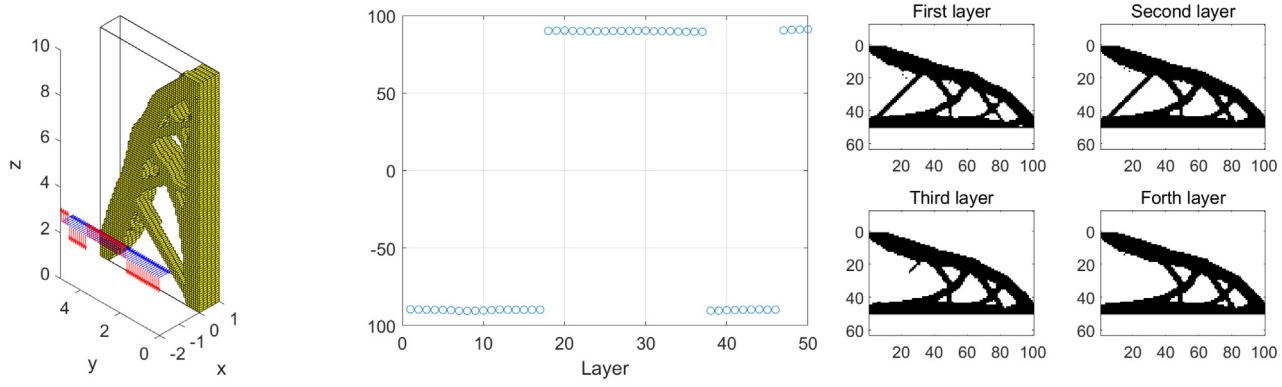

(c) Overhang constraint: 60°

Fig. 16. The optimization results with the shadow density filters for the overhang constraints. (a) The result with 30° shadow density filter, (b) the result with 45° shadow density filter, and (c) the result with 60° shadow density filter.

cess without the shadow density filter is carried out for the optimization result in Fig. 15(b). The optimized design and the optimized raster angles, i.e., the rotation angle of each layer in the y-direction, are plotted with the same manner of the previous examples. The topologically optimized structure which resists the load can be obtained. Interestingly, it is noted that the raster angles become switched in the middle of the optimized layout. It is due to the symmetricity of the material constitutive matrix and the boundary condition. In other words, the raster angles about 90° and −90° are the rotational angles at the middle of the section in Fig. 15(b:right). As the Young's moduli are set $E_2 = 2 \times E_1 = 2 \times E_3$, the rotations in the positive y direction and the negative y direction result in the same stiffness matrix. It also reveals that the structural optimization with the raster angle expands the design space in which the optimizer should explore. Fig. 15(c) shows the filtered and postprocesssed designs. As expected, the left-bottom structural members are removed due to the geometric constraints imposed by the self-supporting condition. The design alternation with the 60° overhang constraint is not significant with the connected boundary condition in the right most design in Fig. 15(c). Unfortunately the structures post-processed with the 30° and 45° overhang constraints are discon-

Table 4
Comparison of optimization designs in Fig. 15 and Fig. 16 (Mass 40 %).

	Optimal design in Fig. 15 and postprocessed designs (J)	Optimal designs in Fig. 16 with the overhang constraint (J)
Without overhang constraint	3.3478×10^4	
Overhang constraint (30°)	1.6184×10^6	1.2360×10^5
Overhang constraint (45°)	1.6203×10^6	1.2016×10^5
Overhang constraint (60°)	3.4051×10^4	3.9490×10^4 (Local optima)

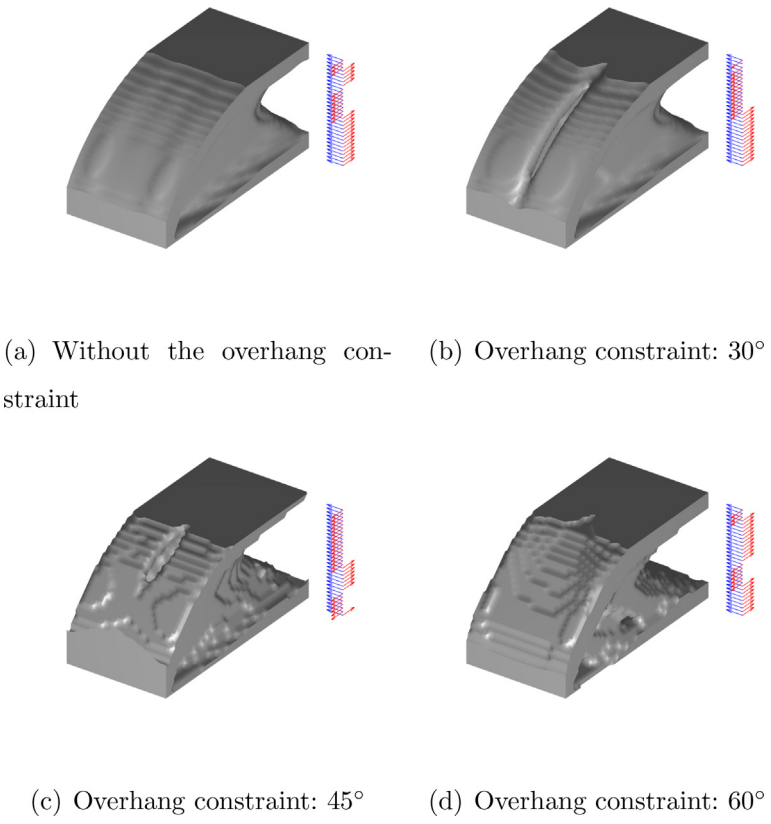

(a) Without the overhang constraint (b) Overhang constraint: 30°

(c) Overhang constraint: 45° (d) Overhang constraint: 60°

Fig. 17. The optimization results for a bigger design domain (30 by 30 by 60). (a) The design without the overhang constraint (compliance: 6.9284×10^3 (J), (b-d) the designs with the overhang constraints (the compliance with the 30° overhang constraint: 7.5407×10^3 (J), the compliance with the 45° overhang constraint: 6.7789×10^3 (J) and the compliance of the 60° overhang constraint: 6.8318×10^3 (J)).

nected and their compliance values are increased significantly. Fig. 16 shows the optimized layouts with the shadow density filter. The optimal layouts satisfying the overhang constraints are obtained as expected. Table 4 compares the compliance values of the optimized layouts in Fig. 15((b) and Fig. 16. As expected, the best design among the compared layouts in Table 4 is the optimization design without any geometric constraint. The design postprocessed with the 60° shadow density filter is the second best design in Table 3 and this implies that the design with the 60° shadow density filter is inferior and it is the local optima issue by the design space restriction by the present shadow density filter. The designs with the 30° and 45° overhang constraints are better than the postprocessed designs of the Fig. 15(b).

3.5. 3 Dimensional example 3: the application of the overhang constraint (Self-supporting structure)

For the next example, the three dimensional problem is considered in Fig. 17. The same procedure of the previous examples is applied. Without the overhang condition, an optimized structure is obtained in Fig. 17(a). Compared with the objective values without the shadow density filter, the lowest objective value can be obtained. With the applications of the shadow density filters, the manufacturing constraints are successfully applied with the increased objective values. The evaluations of the objective values of the design postprocessed by the shadow density filters are not computed as the volumes are also increased significantly. To solve this example, the iterative solver implemented in the Matlab is used to save the computational time and memory. The sensitivity analysis takes about a half of the computation time as it requires the recursive operations of the shadow density filter.

4. Conclusions

This research presents a new shadow density filter method satisfying the overhang constraint or the self-supporting condition and presents its application for structural topology optimization minimizing the compliance subject to the mass constraint by optimizing the raster angles as well as the structural topology. The present research intends to address the importance of the

consideration of the anisotropicity of printed parts. As printed mechanical parts inherently contain the anisotropic material properties, these raster angles can be optimized simultaneously. The optimized raster angles and optimized structures enhance the structural performance. In addition, this research presents the simple algebra to impose the overhang constraints in structural optimization what is catagorized as the density filter method. The shadow density filter developed here simulates the absorption of the light emitted from a bulb. By controlling the absorption direction and depth, it is found that the shadow density filter can be used to impose the overhang constraint in topology optimization. By optimizing the raster angles of each layer that are the printing directions in the additive manufacturing as the design variable, it is possible to find out optimal layouts as well as optimal raster angles considering the anisotropicity. Several numerical examples are solved to demonstrate the validity and effectiveness of the present shadow density filter. For future research, we expect that the present framework can be extended to consider more complex manufacturing constraints. In addition, the optimization of the crust in the additive manufacturing can be considered.

Declaration of Competing Interest

The authors declare that they have no known competing financial interests or personal relationships that could have appeared to influence the work reported in this paper.

Acknowledgement

This work was supported by the National Research Foundation of Korea (NRF) grant funded by the Korea government (MSIT) (NRF-2019R1A2C2084974).

References

[1] Dede EM, Joshi SN, Zhou F. Topology optimization, additive layer manufacturing, and experimental testing of an air-cooled heat sink. J Mech Des 2015;137(11).
[2] Garaigordobil A, Ansola R, Vegueria E, Fernandez I. Overhang constraint for topology optimization of self-supported compliant mechanisms considering additive manufacturing. Comput Aided Des 2019;109:33–48.
[3] Langelaar M. Topology optimization of 3d self-supporting structures for additive manufacturing. Additive Manuf 2016;12:60–70.
[4] Liu JK, Gaynor AT, Chen SK, Kang Z, Suresh K, Takezawa A, et al. Current and future trends in topology optimization for additive manufacturing. Struct Multidiscipl Optimiz 2018;57(6):2457–83.
[5] Zhu J, Zhou H, Wang C, Zhou L, Yuan S, Zhang W. A review of topology optimization for additive manufacturing: Status and challenges. Chinese Journal of Aeronautics 2021;34(1):91–110.
[6] Zhang KQ, Cheng GD, Xu L. Topology optimization considering overhang constraint in additive manufacturing. Comput Struct 2019;212:86–100.
[7] Thore CJ, Grundstrom HA, Torstenfelt B, Klarbring A. Penalty regulation of overhang in topology optimization for additive manufacturing. Struct Multidiscipl Optimiz 2019;60(1):59–67.
[8] Sossou G, Demoly F, Montavon G, Gomes S. An additive manufacturing oriented design approach to mechanical assemblies. J Comput Des Eng 2021;235(3):555–67. https://doi.org/10.1177/0954405420949209. https://www.sciencedirect.com/science/article/pii/S2288430017300659.
[9] Bruggi M, Laghi V, Trombetti T. Simultaneous design of the topology and the build orientation of wire-and-arc additively manufactured structural elements. Comput Struct 2021;242:106370.
[10] Dapogny C, Estevez R, Faure A, Michailidis G. Shape and topology optimization considering anisotropic features induced by additive manufacturing processes. Comput Methods Appl Mech Eng 2019;344:626–65.
[11] Yoon GH, Ha SI. A New Development of a Shadow Density Filter for Manufacturing Constraint and Its Applications to Multiphysics Topology Optimization. J Mech Des 2021;143(6):061703.
[12] Leary M, Merli L, Torti F, Mazur M, Brandt M. Optimal topology for additive manufacture: A method for enabling additive manufacture of support-free optimal structures. Mater Des 2014;63:678–90.
[13] Langelaar M. An additive manufacturing filter for topology optimization of print-ready designs. Struct Multidiscipl Optimiz 2017;55(3):871–83.
[14] Mirzendehdel AM. Support structure constrained topology optimization for additive manufacturing. Comput Aided Des 2016;81:1–30.
[15] Barroqueiro B, Andrade-Campos A, Valente RAF. Designing self supported slm structures via topology optimization. J Manuf Mater Process 2019;3(3). https://doi.org/10.3390/jmmp3030068. https://www.mdpi.com/2504-4494/3/3/68.
[16] Zegard T, Paulino GH. Bridging topology optimization and additive manufacturing. Struct Multidiscipl Optimiz 2016;53:175–92.
[17] Junk S, Klerch B, Nasdala L, Hochberg U. Topology optimization for additive manufacturing using a component of a humanoid robot. Procedia CIRP 2018;70:102–7. https://doi.org/10.1016/j.procir.2018.03.270. 28th CIRP Design Conference 2018, 23–25 May 2018, Nantes, France. https://www.sciencedirect.com/science/article/pii/S2212827118304438.
[18] Gebisa AW, Lemu HG. A case study on topology optimized design for additive manufacturing. IOP Conf Ser: Mater Sci Eng 2017;276:012026. https://doi.org/10.1088/1757-899x/276/1/012026.
[19] Leary M, Merli L, Torti F, Mazur M, Brandt M. Optimal topology for additive manufacture: A method for enabling additive manufacture of support-free optimal structures. Mater Des 2014;63:678–90.
[20] Gaynor AT, Guest JK. Topology optimization considering overhang constraints: Eliminating sacrificial support material in additive manufacturing through design. Struct Multidiscipl Optimiz 2016;54(5):1157–72.
[21] Mantovani S, Campo GA, Ferrari A. Additive manufacturing and topology optimization: A design strategy for a steering column mounting bracket considering overhang constraints. Proc Inst Mech Eng Part C J Mech Eng Sci 2021;235(10):1703–23.
[22] Qian X. Undercut and overhang angle control in topology optimization: A density gradient based integral approach. Int J Numer Meth Eng 2017;111(3):247–72.
[23] Garaigordobil A, Ansola R, Veguería E, Fernandez I. Overhang constraint for topology optimization of self-supported compliant mechanisms considering additive manufacturing. Comput Aided Des 2019;109:33–48.
[24] Guo X, Zhou JH, Zhang WS, Du ZL, Liu C, Liu Y. Self-supporting structure design in additive manufacturing through explicit topology optimization. Comput Methods Appl Mech Eng 2017;323:27–63.
[25] Clausen A, Aage N, Sigmund O. Exploiting additive manufacturing infill in topology optimization for improved buckling load. Engineering 2016;2(2):250–7.
[26] Bower AF. Applied mechanics of solids. http://solidmechanics.org [accessed: 2010-09-30].
[27] Cowin SC. Continuum Mechanics of Anisotropic Materials; 2013.
[28] Yoon G, Kim YY. The role of s-shape mapping functions in the simp approach for topology optimization. KSME Int J 2003;17:1496–506.
[29] Svanberg K. The method of moving asymptotes – a new method for structural optimization. Int J Numer Meth Eng 1987;24(2):359–73.